ECS Journal of Solid State Science and Technology, **3** (12) R238-R244 (2014)
2162-8769/2014/3(12)/R238/7/$31.00 © The Electrochemical Society

Photoluminescence Properties of Eu^{3+} in $Ga_2O_3-Tb_3Ga_5O_{12}:Cr^{3+}$ Phosphor Synthesized by Metal Organic Deposition

Kenji Sawada and Sadao Adachi*,z

Graduate School of Science and Engineering, Gunma University, Kiryu, Gunma 376–8515, Japan

We demonstrated the synthesis of Eu^{3+}-activated $Tb_3Ga_5O_{12}$ garnet phosphor by metal-organic deposition and reported the photoluminescence (PL) properties of this garnet phosphor in detail. The phosphors were synthesized from a mixture of organic gallium solution and acetic acid dissolved with $TbCl_3/Eu_2O_3$. The X-ray diffraction analysis indicated that the synthesized phosphors were a mixture of β-phase Ga_2O_3 and cubic $Tb_3Ga_5O_{12}$ garnet (TGG). The TGG fraction increased with the increase of the $TbCl_3$ addition in the raw solution. The Eu^{3+} ions were preferentially incorporated into the TGG crystallites rather than β-Ga_2O_3. The intensities of the Eu^{3+} emissions in TGG were strongly influenced by the Cr^{3+} red-line emissions, where the Cr^{3+} ions were unintentionally introduced in the synthesized phosphors. The PL excitation spectra indicated that the Eu^{3+} emission at 708 nm ($^5D_0 \rightarrow {}^7F_4$) was gained by the Tb^{3+} intra-*f*-shell, Cr^{3+} intra-*d*-shell, and charge transfer transitions. Temperature dependences of the Eu^{3+} and Cr^{3+} emission intensities were measured at $T = 20 - 380$ K and explained by the proposed theoretical models very well. The effects of the Eu^{3+} ion site in the various host materials on the luminous properties were also discussed in detail.
 [DOI: 10.1149/2.0071412jss]

Manuscript submitted September 8, 2014; revised manuscript received October 1, 2014. Published October 11, 2014.

Monoclinic gallium oxide (β-Ga_2O_3) is a wide band-gap semiconductor (∼4.7 eV at 300 K)[1] with an *n*-type conductivity when slightly oxygen deficient. β-Ga_2O_3 has also a good chemical, thermal, and mechanical stability. Thus, it has been used as electroluminescent devices,[2] Schottky barrier devices,[3] field-effect transistors,[4] heterojunction UV detectors,[5] high-temperature gas (O_2, H_2, CO, CH_4, etc.) sensors,[6] humidity sensors,[7] solar-blind photodetectors,[8] capping/passivation coatings,[9] transparent conducting oxides,[10] and photocatalysis.[11]

Recently, we demonstrated a method for synthesizing red-, orange-, and green-emitting β-Ga_2O_3 phosphors using a newly developed method, namely, the metal organic deposition (MOD).[12–14] The schematic energy-level diagrams of the trivalent ions, Cr^{3+}, Eu^{3+}, and Tb^{3+}, in the β-Ga_2O_3 host were also proposed for the sake of a better understanding of the luminous properties of these trivalent ion-activated phosphors.[12–14] The success in synthesizing Cr^{3+}-, Eu^{3+}-, and Tb^{3+}-activated β-Ga_2O_3 phosphors further encourages to challenge in synthesizing β-Ga_2O_3 phosphors codoped with the multiple ions.

As a series, the rare-earth gallium garnets serve as important host crystals for numerous spectroscopic and magnetic studies on the trivalent rare-earth ions, and some of the strongest magneto-optical effects have been observed in rare-earth gallium garnets, especially when the rare-earth ion is Tb^{3+}.[15] The melting point of terbium gallium garnet phosphor (TGG) is ∼1725°C. Although TGG can be synthesized by the Czochralski technique,[16] its growth is not exempt of difficulties. The decomposition and evaporation of gallium-sesquioxide from the melt leads to a continuous shift of the melting point and composition of the bulk crystal. Note that the MOD method is a low-temperature synthesis technique (≤1200°C).[12–14]

The purpose of this study is twofold: (i) to demonstrate the synthesis of Eu^{3+}-activated $Tb_3Ga_5O_{12}$ garnet phosphor (TGG:Eu^{3+}) by the MOD and (ii) to systematically investigate the optical properties of this phosphor using photoluminescence (PL) analysis and PL excitation (PLE) spectroscopy. It is found that surprisingly, the MOD method enables to synthesize TGG:Eu^{3+}, rather than (Tb^{3+}, Eu^{3+})-codoped Ga_2O_3 phosphor, by adding Tb^{3+}/Eu^{3+} in the gallium oxide raw material.

To the best of our knowledge, the PL properties of TGG:Eu^{3+} phosphor have not been reported until now. We show that TGG:Eu^{3+} is an exceptionally efficient phosphor emitting in the red spectral region (∼600 − 700 nm). A particularly interesting coupled-ion process was previously reported in the emission spectrum of Cr^{3+}-doped $Eu_3Ga_5O_{12}$.[17] Because the level structure of Cr^{3+} is well known, and the Eu^{3+} ion has a number of properties unique among rare-earth ions, the $Cr^{3+}-Eu^{3+}$ system seems to be exceedingly amenable for detailed investigation. Thus, we pay attention on the effects of the Cr^{3+} ions, which were unintentionally doped into the MOD-synthesized Ga_2O_3-TGG phosphors, on their PL properties.

Experimental

The Ga_2O_3-TGG:Eu^{3+} powders were prepared by thermal decomposition, namely, MOD. A mixture of $Ga(RCOO)_n$, $CH_3OOC_2H_5$, turpentine, and $C_xH_yO_z$ (Ga-03) was supplied from Kojundo Chemical Laboratory Co., Ltd., Japan, and used as the starting solution. This solution was previously used as the raw source for various trivalent ion-activated β-Ga_2O_3 phosphors (Cr^{3+}, Eu^{3+}, and Tb^{3+}).[12–14] First, $TbCl_3$ and Eu_2O_3 were dissolved in an aqueous CH_3COOH solution. Then, this solution was mixed with the MOD solution. The mixed raw solution was Ga : Tb : Eu = 1 : *M* : *N* in molar ratio. A gelatinous material was obtained by stirring the mixed raw solution. After prebaking in air at 120°C for 10 min, the phosphor precursor was calcined on an alumina boat at 1200°C for 30 min in flowing dry O_2 atmosphere. The phosphor powders were finally grained in an agate mortar.

The structural properties of the MOD-synthesized phosphors were characterized by X-ray diffraction (XRD) analysis using a RAD-IIC X-ray diffractometer (Rigaku) with Cu *K*α radiation. PL measurements were performed using a spectrometer equipped with a charge-coupled device (Princeton Instruments PIXIS 100) and a He−Cd laser at λ = 325 nm (Kimmon IK3302R-E) as the excitation light source at temperatures between $T = 20$ and 380 K. PL spectra were corrected for the sensitivities of the detection system. PLE measurements were performed using a 200 W xenon lamp as the excitation light source combined with a monochromator (JASCO CT-25C) and a Peltier-device-cooled photomultiplier tube (Hamamatsu R375). PLE spectra were corrected for the xenon lamp intensity and the sensitivities of the detection system.

Results

Structural properties.— Figure 1a shows the XRD patterns obtained from the samples synthesized at $M = 0.01$, 0.10, and 0.30 with $N = 0.0003$ and subsequently calcined at $T_c = 1200$°C for $t = 30$ min, where *M* and *N* are Tb and Eu concentrations in molar ratio, respectively. The XRD traces for the MOD-synthesized Ga_2O_3 powders calcined below 700°C usually showed no clear crystallographic peaks.[12,13] Calcining above 800°C, weak crystallographic peaks at $2\theta \sim 30 - 40°$ were observed. Many strong XRD peaks were observed for the crystalline Ga_2O_3 samples calcined at $T_c \geq 1000$°C.[12,13]

*Electrochemical Society Active Member.
zE-mail: adachi@el.gunma-u.ac.jp

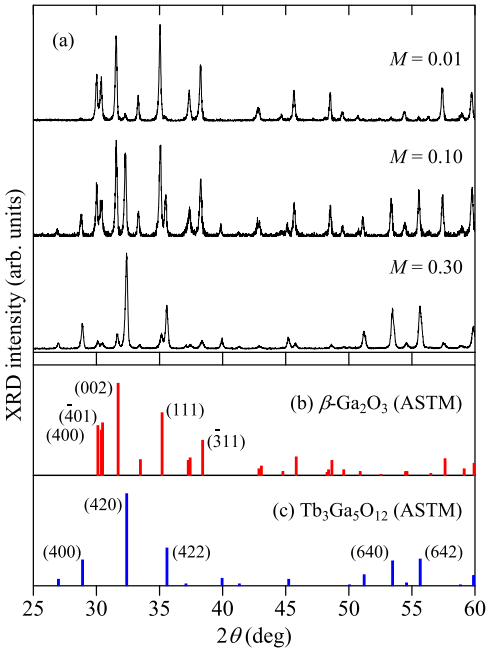

Figure 1. (a) XRD traces of $Ga_2O_3-TGG:Eu^{3+}$ phosphors. The samples were synthesized at $M = 0.01$, 0.10, and 0.30 (Tb^{3+}) with $N = 0.0003$ (Eu^{3+}) and subsequently calcined at $T_c = 1200°C$ for $t = 30$ min in dry O_2 atmosphere. The ASTM card patterns for monoclinic β-Ga_2O_3 (#00-041-1103) and cubic $Tb_3Ga_5O_{12}$ (#01-088-0575) are shown in (b) and (c), respectively.

In Fig. 1a, the dominant diffraction peaks for the sample synthesized with $M = 0.01$ come from monoclinic Ga_2O_3 structure (β-Ga_2O_3) with the space group of $C_{2h}^3 - C2/m$.[18] The XRD pattern of β-Ga_2O_3, taken from the American Society for Testing and Materials (ASTM) card (#00-041-1103), is shown in Fig. 1b. For the sample synthesized with $M = 0.30$, the XRD pattern is clearly different from that of β-Ga_2O_3. We found that it corresponds to the trace of cubic TGG with the space group of $O_h^{10} - Ia\bar{3}d$.[19] The XRD pattern of cubic TGG, taken from the ASTM card (#01-088-0575), is shown in Fig. 1c. We can conclude from Fig. 1 that our MOD-synthesized phosphors contain the two different crystalline phases, β-Ga_2O_3 and cubic TGG.

The XRD results in Fig. 1a indicate that the fraction of cubic TGG increases as the amount of $TbCl_3$ (M value) in the starting solution is increased. Let us define the following expression to estimate the β-Ga_2O_3 fraction in a Ga_2O_3-TGG mixture:

$$f_G = 1 - f_T = \frac{\sum_i I_{i,G}}{\sum_i I_{i,G} + \sum_j I_{j,T}} \quad [1]$$

where f_G (f_T) represents the β-Ga_2O_3 (TGG) fraction in the powder mixture while $I_{i,G}$ ($I_{j,T}$) refers to the measured diffraction intensity of the ith (jth) crystallographic plane. Here, we consider the diffraction planes of (400), ($\bar{4}01$) , (002), (111), and ($\bar{3}11$) for the ith planes (β-Ga_2O_3) and (400), (420), (422), (640), and (642) for the jth planes (TGG) (see Figs. 1b and 1c).

The f_G versus Tb content (M) plots for the MOD-synthesized samples with $N = 0.0003$ are shown in Fig. 2. As can be expected, we obtained $f_G = 1.0$ for the sample synthesized without adding $TbCl_3$ (i.e., $M = 0$). For $M = 0.01$, we obtained $f_G \sim 0.94$ and $f_T \sim 0.06$. The f_G value was gradually decreased with the increase of M. We also obtained $f_G \sim 0.17$ at $M = 0.3$. The solid line in Fig. 2 represents the result calculated using

$$f_G = 1.0 \exp(-6.2M) \quad [2]$$

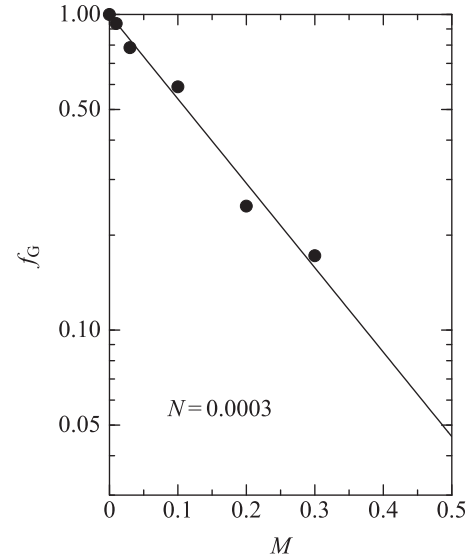

Figure 2. Monoclinic Ga_2O_3 (β-Ga_2O_3) fraction f_G vs M for $Ga_2O_3-TGG:Eu^{3+}$ phosphors. The samples were synthesized at $M = 0$ to 0.30 (Tb^{3+}) with $N = 0.0003$ (Eu^{3+}). The β-Ga_2O_3 fractions f_G were determined from the XRD traces using Eq. 1. The solid line shows the result calculated using Eq. 2.

PL spectra of specific samples.— Figure 3 shows the PL spectra for (a) undoped β-Ga_2O_3, (b) β-$Ga_2O_3:Tb^{3+}$, (c) β-$Ga_2O_3:Eu^{3+}$, and (d) $Ga_2O_3-TGG:Eu^{3+}$ phosphors measured at $T = 20$ and 300 K. These phosphors were synthesized with (a) $M = N = 0$, (b) $M = 0.01$ and $N = 0$, (c) $M = 0$ and $N = 0.0003$, and (d) $M = 0.01$ and $N = 0.0003$. All these samples were calcined at $T_c = 1200°C$ for $t = 30$ min.

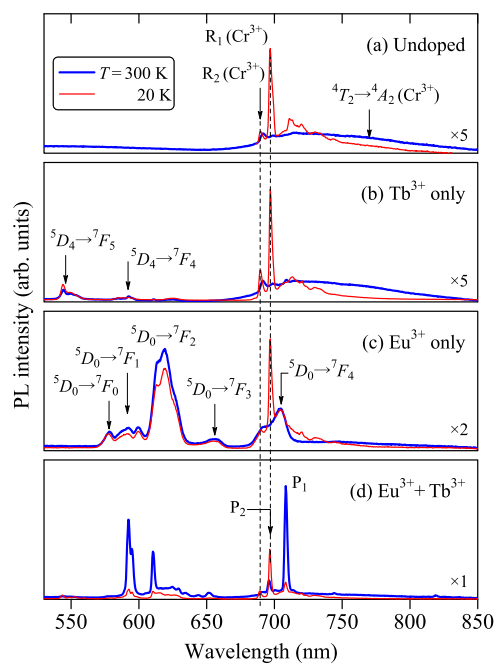

Figure 3. PL spectra for (a) undoped β-Ga_2O_3, (b) β-$Ga_2O_3:Tb^{3+}$, (c) β-$Ga_2O_3:Eu^{3+}$, and (d) $Ga_2O_3-TGG:Eu^{3+}$ phosphors measured at $T = 20$ and 300 K by excitation at $\lambda_{ex} = 325$ nm (He−Cd laser). The samples were synthesized with (a) ($M = 0$, $N = 0$), (b) ($M = 0.01$, $N = 0$), (c) ($M = 0$, $N = 0.0003$), and (d) ($M = 0.01$, $N = 0.0003$) and subsequently calcined at $T_c = 1200°C$ for $t = 30$ min in dry O_2 atmosphere. The strongest PL intensity was observed from (d) (notice magnifications in each figure).

The PL spectra of the undoped β-Ga_2O_3 sample in Fig. 3a exhibit a deep-red emission band peaking at ∼730 nm, together with two sharp red emission peaks R_1 and R_2 at ∼1.78 and ∼1.80 eV, respectively. These deep-red emission band and two sharp red emission peaks (R_1 and R_2) can be attributed to the $^4T_2 \rightarrow {}^4A_2$ and $^2E \rightarrow {}^4A_2$ transitions of Cr^{3+} ions in β-Ga_2O_3,[12] respectively. Such deep-red and sharp red emissions are commonly observed in Al_2O_3:Cr^{3+} (ruby) and Ga_2O_3:Cr^{3+}. Note that the Cr^{3+} ions were accidentally or naturally introduced in our synthesized samples. It has been reported that very low concentrations, an order of ppm, of Cr^{3+} in Ga_2O_3 result in the strong deep-red luminescence band and sharp red emission peaks.[20–22] Moreover, Cr atoms were reported to be unintentionally doped into Ga_2O_3 crystals as contaminant.[20,21] Major components of this contamination may be tweezers, beakers, furnace boats, furnace tube walls, and so on. Detailed luminescence properties of Ga_2O_3:Cr^{3+} can be found in Ref. 12.

The PL spectra in Fig. 3b show a series of the weak peaks at ∼540, ∼590, and ∼620 nm. These peaks are attributed to the $^5D_4 \rightarrow {}^7F_5$ (∼540 nm), $^5D_4 \rightarrow {}^7F_4$ (∼590 nm), and $^5D_4 \rightarrow {}^7F_3$ (∼620 nm) transitions in Tb^{3+}.[14] As in Fig. 3a, the Cr^{3+}-originated R_1 emission intensity greatly enhances at $T = 20$ K. No strong temperature dependence of the PL intensity of the Tb^{3+}-related emission peaks has, however, been observed in the β-Ga_2O_3 host. Since no strong thermal activation of the unintentionally doped Cr^{3+} ions occurs in β-Ga_2O_3 when calcined at low temperatures ($T_c \leq 700°C$),[12] the β-Ga_2O_3:Tb^{3+} samples synthesized by the MOD and subsequently calcined at ∼700°C showed only the Tb^3-related emission dominated PL spectra.[14]

The PL spectrum of β-Ga_2O_3:Eu^{3+} at $T = 300$ K in Fig. 3c shows the well-characterized Eu^{3+} emission peaks at ∼580 nm ($^5D_0 \rightarrow {}^7F_0$), ∼590 nm ($^5D_0 \rightarrow {}^7F_1$), ∼620 nm ($^5D_0 \rightarrow {}^7F_2$), ∼655 nm ($^5D_0 \rightarrow {}^7F_3$), and ∼705 nm ($^5D_0 \rightarrow {}^7F_4$).[13] Like the Tb^{3+}-related peaks (Fig. 3b), these Eu^{3+}-related peaks show no strong temperature dependence of the PL intensities between $T = 20$ and 300 K. However, the Cr^{3+} R_1 peak is observed to be dominated in the PL spectrum at $T = 20$ K.

The Ga_2O_3−TGG:Eu^{3+} phosphor in Fig. 3d shows the quite unique PL spectra. These spectra exhibit very sharp peaks at ∼590, ∼610, ∼695, and ∼710 nm. It is also found that the emission intensities of these peaks are strongly dependent on temperature T. As we will see in the following, these sharp emission peaks, regardless of $T = 20$ or 300 K, are due to the intra-*f*-shell transitions of Eu^{3+} in the cubic TGG host. In Fig. 3, the strongest PL peak intensity is observed from the Ga_2O_3−TGG:Eu^{3+} phosphor at $T = 300$ K (Fig. 3d) and the next strongest PL peak intensity is from the β-Ga_2O_3:Eu^{3+} phosphor at $T = 20$ K (or 300 K) (Fig. 3c).

PL spectra: Eu^{3+} concentration dependence.— Figure 4 shows the PL spectra of the MOD-synthesized phosphors with N varying from 0 to 0.1 at $M = 0.01$ measured at room temperature. The XRD measurements indicated that the fractions (f_G) of β-Ga_2O_3 for these phosphors are ∼0.94 (see also Fig. 2). It is thus understand that the Ga_2O_3−TGG:Eu^{3+} phosphors synthesized with $M = 0.01$ and $N = 0 - 0.1$ in Fig. 4 are dominated by β-Ga_2O_3; only a few percent are cubic TGG crystallites ($f_T \sim 0.06$).

As expected, no strong Eu^{3+}-related emission peak can be observed in the PL spectrum of the sample synthesized with $N = 0$. The Eu^{3+}-related sharp emission peaks appear, increase in their intensity with increasing N, and show a maximum at $N = 0.0003$. At $N \geq 0.01$, the relatively broad Eu^{3+} emission peaks, which were typically observed in monoclinic Ga_2O_3 (β-Ga_2O_3),[13] appear to dominate.

The intensity of the Eu^{3+} emission peak at ∼620 nm ($^5D_0 \rightarrow {}^7F_2$), which was typically observed in β-Ga_2O_3:Eu^{3+} phosphors, and those for the Eu^{3+} emission peaks at 708 nm (P_1; $^5D_0 \rightarrow {}^7F_4$) and 592 nm ($^5D_0 \rightarrow {}^7F_1$), versus N concentration for the MOD-synthesized phosphors are shown in Fig. 5. These emission intensities (I_{PL}) were calculated by integrating the PL spectra in Fig. 4. We can see that the Eu^{3+} emissions at 708 nm (P_1) and 592 nm exhibit a gradual increase with logarithmic increase in N, showing a maximum at $N \sim 0.0003$. The intensity of the $^5D_0 \rightarrow {}^7F_2$ emissions at ∼620 nm also shows an increase with the increase of N. This dependence of I_{PL} on N is quite similar to that observed in Tb^{3+}-activated β-Ga_2O_3 phosphor (Fig. 3 in Ref. 14). Thus, we can conclude that the "broad" Eu^{3+}-related emission peaks dominantly observed at $N \geq 0.01$ are due to Eu^{3+} introduced into the β-Ga_2O_3 crystallites of the Ga_2O_3−TGG:Eu^{3+} phosphor. The Eu^{3+} ions introduced into the cubic TGG crystallites must give the "sharp" emission peaks in the PL spectra. Detailed spectral features of the Eu^{3+} emissions will be discussed in Crystal symmetry and Eu^{3+} emission spectrum subsection in the Discussion section.

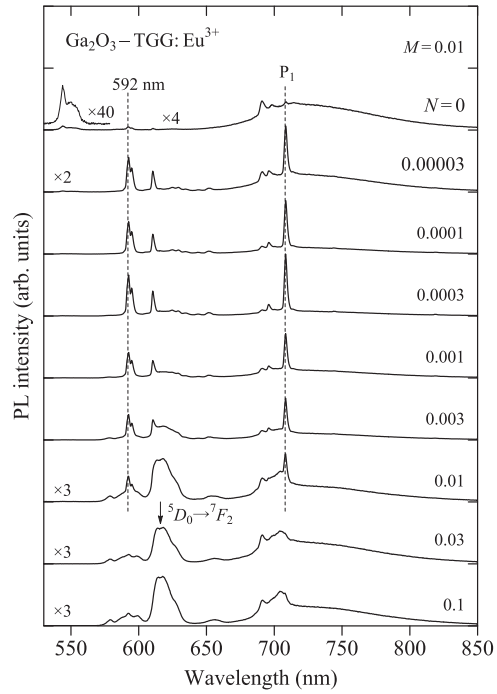

Figure 4. Room-temperature PL spectra for the Ga_2O_3−TGG:Eu^{3+} phosphors synthesized at $N = 0 - 0.1$ (Eu^{3+}) with $M = 0.01$ (Tb^{3+}).

PLE spectra.— Figure 6 shows the PL and PLE spectra of (a) TGG:Eu^{3+} (Ga_2O_3−TGG:Eu^{3+}), (b) β-Ga_2O_3:Eu^{3+}, (c) β-Ga_2O_3:Tb^{3+}, and (d) undoped β-Ga_2O_3 phosphors measured at $T = 300$ K. The PL spectra, the same as those in Fig. 3, were measured by excitation at $\lambda_{ex} = 325$ nm (He−Cd laser), while the PLE spectra were obtained by monitoring at (a) $\lambda_{em} \sim 592$ nm [Eu^{3+} ($^5D_0 \rightarrow {}^7F_1$)]

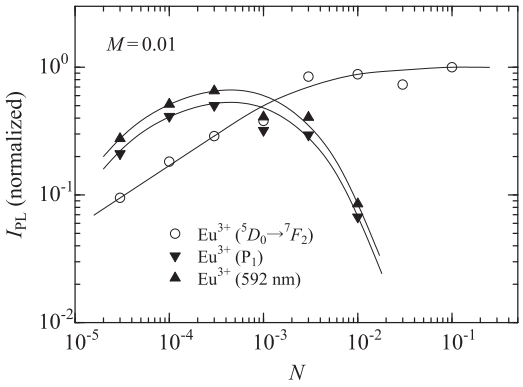

Figure 5. Integrated PL intensities (I_{PL}) of the Eu^{3+} emission peaks at ∼620 nm ($^5D_0 \rightarrow {}^7F_2$), at 708 nm ($P_1$; $^5D_0 \rightarrow {}^7F_4$), and at 592 nm ($^5D_0 \rightarrow {}^7F_1$) versus N concentration (Eu^{3+}) for the Ga_2O_3−TGG:Eu^{3+} phosphors synthesized with $M = 0.01$ (Tb^{3+}). The I_{PL} data were obtained by integrating the PL spectra in Fig. 4. Note that the Eu^{3+} emission peak at ∼620 nm ($^5D_0 \rightarrow {}^7F_2$) is typically observed in β-Ga_2O_3:Eu^{3+} phosphors.

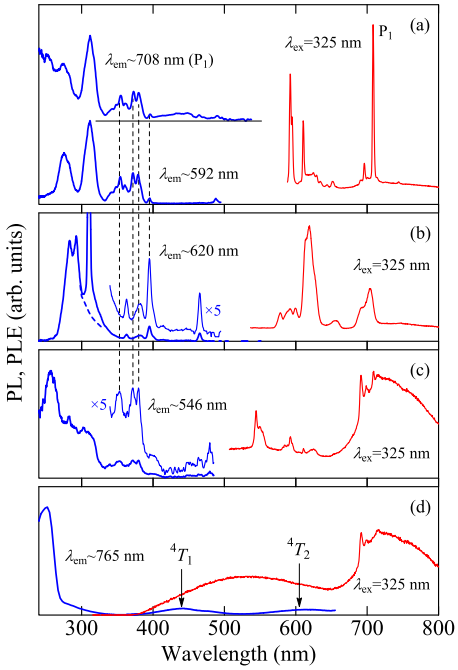

Figure 6. PL and PLE spectra of (a) TGG:Eu^{3+} (Ga_2O_3−TGG:Eu^{3+}), (b) β-Ga_2O_3:Eu^{3+}, (c) β-Ga_2O_3:Tb^{3+}, and (d) undoped β-Ga_2O_3 phosphors measured at $T = 300$ K. Note that the strong and sharp peak observed at ∼310 nm in (b) comes from the second-order diffraction on the spectrometer grating of the monitored PL light ($\lambda_{em}/2 \sim 310$ nm).

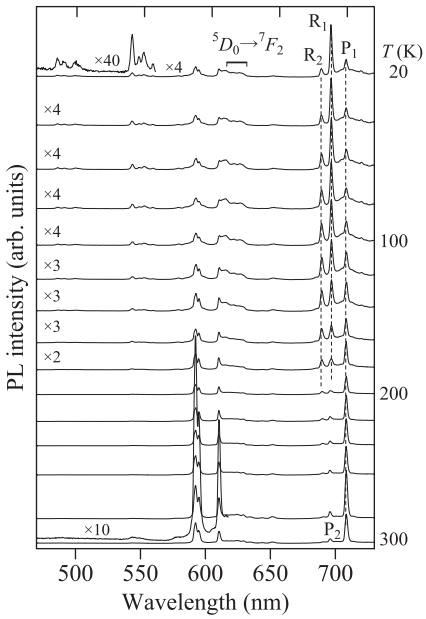

Figure 7. PL spectra for the Ga_2O_3−TGG:Eu^{3+} phosphor synthesized with $M = 0.01$ (Tb^{3+}) and $N = 0.0003$ (Eu^{3+}) measured between $T = 20$ and 300 K in 20 K increments.

and ∼708 nm [Eu^{3+} P_1 ($^5D_0 \rightarrow {}^7F_4$)], (b) $\lambda_{em} \sim 620$ nm [Eu^{3+} ($^5D_0 \rightarrow {}^7F_2$)], (c) $\lambda_{em} \sim 546$ nm [Tb^{3+} ($^5D_4 \rightarrow {}^7F_5$)], and (d) $\lambda_{em} \sim 765$ nm [Cr^{3+} ($^4T_2 \rightarrow {}^4A_2$)]. It should be noted that the strong and sharp PLE peak at ∼310 nm in Fig. 6b comes from the second-order diffraction on the spectrometer grating of the monitored PL light ($\lambda_{em}/2 \sim 310$ nm). The large broad emission band peaking at ∼530 nm in Fig. 6d may be related to a structural defect or an impurity level within the bandgap of β-Ga_2O_3.

The PLE spectrum for the TGG:Eu^{3+} phosphor monitored at $\lambda_{em} \sim 708$ nm is quite different from that obtained by monitoring at $\lambda_{em} \sim 592$ nm (Fig. 6a). It is found that the ∼708 nm emission is gained by the Cr^{3+} ($^4A_2 \rightarrow {}^4T_2$) excitation transitions at $\lambda \sim 400 - 500$ nm (Fig. 6d, see also Ref. 12). This gained emission reflects an energy transfer occurring from Cr^{3+} to Eu^{3+}. Figure 6a also indicates that the excitation at $\lambda < 260$ nm is more efficient for the ∼708 nm emission (P_1) than for the ∼592 nm emission. This fact suggests that the more efficient charge transfer occurs between O^{2-} in TGG (or TGG via β-Ga_2O_3) and lower-state $^7F_4$ (Eu^{3+}) than between O^{2-} and higher-state $^7F_1$ (Eu^{3+}).

The sharp PLE peaks observed at $\lambda \sim 330 - 385$ nm in Fig. 6c are due to absorbing transitions from the Tb^{3+} $^7F_0$ ground state to the Tb^{3+} ^5D_I ($I = 0 - 3$) excited states.[14] These sharp peaks can also be found in the PLE spectra of the Eu^{3+} emissions (∼592 and ∼708 nm) in Fig. 6a, indicating an energy transfer of $Tb^{3+} \rightarrow Eu^{3+}$ in the TGG ($Tb_3Ga_5O_{12}$):Eu^{3+} phosphor.

PL spectra: Temperature dependence.— Figure 7 shows the temperature dependence of the PL spectra for the Ga_2O_3−TGG:Eu^{3+} phosphor synthesized with $M = 0.01$ and $N = 0.0003$. It is observed that the overall PL intensity increases with increasing T for $20 \leq T \leq 280$ K. Below $T \sim 200$ K, the Cr^{3+}-originated R_1 and R_2 peaks dominate. The Eu^{3+}-related emission intensities are also found to be stronger at higher temperatures.

Figure 8 shows the temperature dependences of the PL intensity for (a) the 592 nm ($^5D_0 \rightarrow {}^7F_1$) emission peak in the TGG crystallites, (b) Eu^{3+}-related broad $^5D_0 \rightarrow {}^7F_1$ emission band at

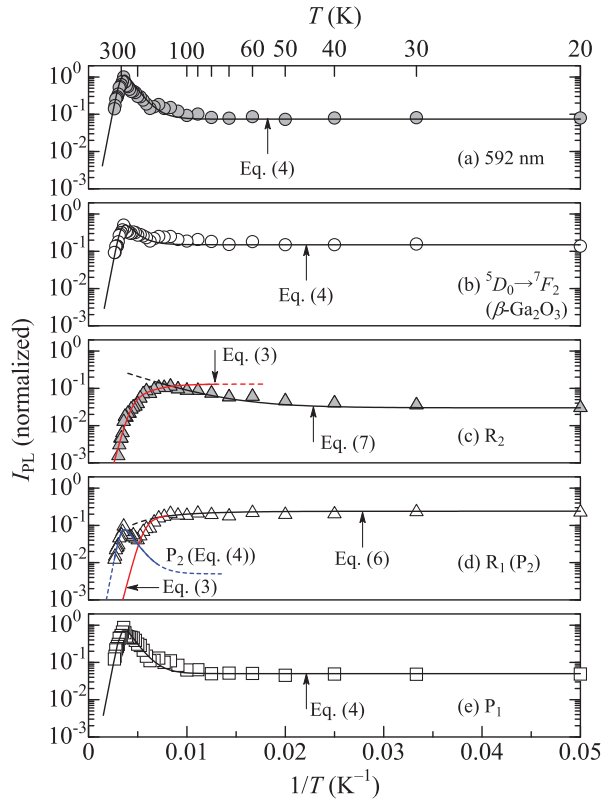

Figure 8. Temperature dependences of the PL intensities for (a) the 592 nm ($^5D_0 \rightarrow {}^7F_1$) emission peak in the TGG crystallites, (b) Eu^{3+}-related broad $^5D_0 \rightarrow {}^7F_1$ emission band at ∼620 nm in the β-Ga_2O_3 crystallites, (c) Cr^{3+} R_1-line emission peak in the TGG/β-Ga_2O_3 crystallites, (d) Cr^{3+} R_2-line emission peak in the TGG/β-Ga_2O_3 crystallites, and (e) Eu^{3+}-related sharp $^5D_0 \rightarrow {}^7F_1$ (P_1) emission peak at 708 nm in the TGG crystallites. Each I_{PL} value was obtained by integrating the PL spectra for the ($M = 0.01$, $N = 0.0003$) sample measured at $T = 20 - 380$ K in 10 K increments (see, e.g., Fig. 7). The solid lines in each figure show the results calculated using Eqs. 3, 4, 6, and 7. The fitting parameters determined here are listed in Table I.

Table I. Fitting parameters used in Eqs. 3, 4, 6, and 7.

Parameter	Eu^{3+}			Cr^{3+}	
	$^5D_0 \rightarrow {}^7F_1$ (592 nm)[a]	$^5D_0 \rightarrow {}^7F_2$ (~620 nm)[b]	$^5D_0 \rightarrow {}^7F_4$ (P_1)[a]	R_1	R_2
I_0	0.074	0.15	0.05	0.22	0.13
a_1	8×10^5	8×10^5	8×10^5	7×10^5	5×10^4
E_{q1} (eV)	0.35	0.35	0.35	0.20	0.20
a_2				20	20
E_{q2} (eV)				0.05	0.05
A_t	550	100	550		
E_t (eV)	0.08	0.08	0.08		
I_R				0.24	0.03
a_R				1.5	
b_R					18
Δ (eV)				0.019	0.019

[a]TGG:Eu^{3+}.
[b]β-Ga_2O_3:Eu^{3+}.

~620 nm in the β-Ga_2O_3 crystallites, (c) Cr^{3+} R_1-line emission peak in the TGG/β-Ga_2O_3 crystallites, (d) Cr^{3+} R_2-line emission peak in the TGG/β-Ga_2O_3 crystallites, and (e) Eu^{3+}-related sharp $^5D_0 \rightarrow {}^7F_1$ (P_1) emission peak at 708 nm in the TGG crystallites. These data were obtained by integrating the PL spectra measured for the ($M = 0.01$, $N = 0.0003$) sample at $T = 20 - 380$ K in 10 K increments.

The decreases in I_{PL} above ~280 K in Figs. 8a, 8b, 8d, and 8e are due to the thermal quenching process usually rationalized by

$$I_{PL}(T) = \frac{I_0}{\sum_i a_i \exp(-E_{qi}/k_B T)} \quad [3]$$

where E_{qi} is the quenching (activation) energy and k_B is the Boltzmann constant. Note, however, that the Eu^{3+}-related emissions in Figs. 8a, 8b, and 8e exhibit an increase in the PL intensity with the increase of T above 20 K. This unique feature cannot be explained by the conventional thermal activation or quenching expression of Eq. 3. Therefore, we consider a simple energy transfer process, which takes place from the host material to Eu^{3+}, by

$$I_{PL}(T) = \frac{I_0}{\sum_i a_i \exp(-E_{qi}/k_B T)} \left[1 + A_t \exp\left(-\frac{E_t}{k_B T}\right)\right] \quad [4]$$

The energy transfer on the second term in the square bracket of Eq. 4 is assumed to be activated by thermal energy of E_t.

The solid lines in Figs. 8a, 8b, and 8e show the results calculated using Eq. 4. The fit-determined parameter values are listed in Table I. We can see that the energy transfer model of Eq. 4 successfully explains the peculiar temperature dependence of the Eu^{3+}-related emission intensities at T below ~280 K. The decrease in I_{PL} observed at T above 280 K can also be well explained by the thermal quenching energy of 0.35 eV.

Lightly Cr-doped alumina (ruby) is well known to emit red light at ~1.78 eV (R_1) and ~1.80 eV (R_2). These R-line emission peaks R_1 and R_2, known as the R-line doublet, are due to the $^2E \rightarrow {}^4A_2$ transition of Cr^{3+} ions in the α-Al_2O_3 (ruby) host. The ^2E state does not split by the sole action of the trigonal field or by the spin−orbit interaction but only by the interplay of these two effects. The splitting energy of the four-fold degenerate state ^2E is written as[23]

$$^2E \quad \begin{cases} \Delta/2 & (2\overline{A}) \\ -\Delta/2 & (\overline{E}) \end{cases} \quad [5]$$

where Δ is in eV and can be determined experimentally (Fig. 3, see also Fig. 7). Note that α-Al_2O_3 is optically uniaxial but β-Ga_2O_3 is biaxial. Therefore, the eigenvalue of the crystal-field and spin−orbit interaction Hamiltonians for β-Ga_2O_3:Cr^{3+} should be slightly different from Eq. 5. Here, we test the hypothesis that the center of gravity of the ^2E state is also at $\pm(\Delta/2)$, as in Eq. 5.

The lower-energy R_1-line emission intensity at $T = 20$ K (Fig. 8d) is about one order stronger than the higher-energy R_2-line one (Fig. 8c), but becomes comparable at ~200 K. This can be explained by the thermal depopulation effect of the R_1 ($\overline{E}$) state, which occurs with increasing T. The thermal depopulation and population in the R_1 ($\overline{E}$) and R_2 ($2\overline{A}$) states can be expressed by the Boltzmann factor $\exp(-\Delta/kT)$ with Δ in Eq. 5. The effect of thermal depopulation in the R_1 ($\overline{E}$) state on its luminescence intensity can be written as

$$I_{PL}(T) = I_R \left[1 - a_R \exp\left(-\frac{\Delta}{k_B T}\right)\right] \quad [6]$$

Similarly, the thermal population-induced PL intensity in the R_2 ($2\overline{A}$) state is given by

$$I_{PL}(T) = I_R \left[1 + b_R \exp\left(-\frac{\Delta}{k_B T}\right)\right] \quad [7]$$

The solid lines in Figs. 8c and 8d show the results calculated using Eqs. 7 and 6, respectively. The fit-determined parameter values are listed in Table I. The splitting energy Δ used here is 19 meV (see Figs. 3 and 7). Our proposed models of Eqs. 6 and 7 can reasonably explain the experimental Cr^{3+} R_1- and R_2-line emission intensities. Above $T \sim 200$ K, the R_1- and R_2-line emission intensities exhibit a strong thermal quenching and can therefore be fitted using Eq. 3 (see parameter values in Table I).

As evidenced from Fig. 3, the Cr^{3+} R_1-line emission occurs at 697 nm, which is just the same as the Eu^{3+} Stark-sublevel P_2 ($^5D_0 \rightarrow {}^7F_4$) emission wavelength. This is only due to a casual coincidence. Thus, the increased I_{PL} at >200 K in Fig. 8d is due to the grow-up P_2 emission component. The solid line in Fig. 8d represents the result calculated using Eq. 4. This expression is the same as that used for the Eu^{3+} Stark-sublevel P_1 ($^5D_0 \rightarrow {}^7F_4$) emission intensity in Fig. 8e.

Discussion

Crystal symmetry and Eu^{3+} emission spectrum.— Figure 9 shows the typical Eu^{3+} emission spectra observed from SnO_2, β-Ga_2O_3, and $Gd_3Ga_5O_{12}$, together with that of TGG. The PL spectra of β-Ga_2O_3:Eu^{3+} and TGG:Eu^{3+} are obtained in the present study, whereas those of SnO_2:Eu^{3+} and $Gd_3Ga_5O_{12}$:Eu^{3+} are taken from Refs. 24 and 25, respectively. Note that SnO_2 crystallizes in a rutile-type, tetragonal structure with the space group $D_{4h}^{14} - P4_2/mnm$, β-Ga_2O_3 crystallizes in the monoclinic structure with the space group of $C_{2h}^3 - C2/m$, and $Gd_3Ga_5O_{12}$ and TGG crystallize in the cubic structure with the space group of $O_h^{10} - Ia\overline{3}d$.

The electronic dipole transitions between 4*f* levels of the rare earth ions are in principle strictly forbidden. The optical transitions between the ^5D_I and ^7F_J levels of the Eu^{3+} ion are also spin prohibition.

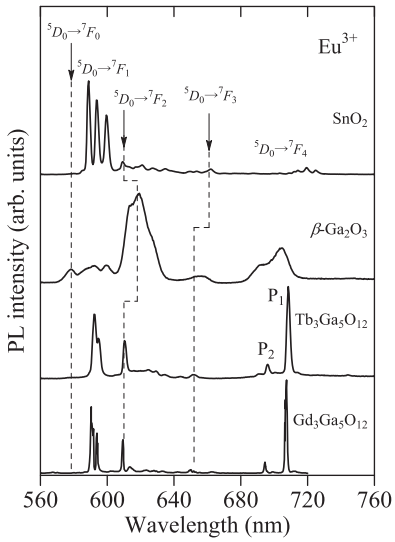

Figure 9. Room-temperature PL spectra for the Eu^{3+}-activated SnO_2, β-Ga_2O_3, and $Gd_3Ga_5O_{12}$ phosphors, together with that for TGG. The PL spectra for β-Ga_2O_3:Eu^{3+} and TGG:Eu^{3+} are measured in the present study, whereas those for SnO_2:Eu^{3+} and $Gd_3Ga_5O_{12}$:Eu^{3+} are taken from Refs. 24 and 25, respectively.

However, this prohibition is not strict because the description of the ^7F_J levels as states with six parallel spins is not entirely correct. The spin−orbit coupling makes ^7F_J state as being composed of a pure ^7F_J state with a slight "admixture" of the pure ^5D_I state. Therefore, the spin prohibition no longer applies so strictly.

The parity prohibition can be lifted only by the influence of the crystal lattice. If Eu^{3+} ion is located at a site that is a center of symmetry in the relevant crystal, then the odd crystal field terms are absent and the parity prohibition can be lifted. In that case, only magnetic-dipole transitions are possible. The corresponding selection rule is: $\Delta J = J - I = 0, \pm 1$ (except that $J = 0 \leftrightarrow I = 0$ is forbidden). In SnO_2:Eu^{3+} where Eu^{3+} is situated at a center of symmetry and is brought into the $^5D_0$ state, the only possible transition accompanied by the emission of radiation is $^5D_0 \rightarrow {}^7F_1$ (magnetic-dipole transition). The sharp triplet lines at ∼590 nm observed in Fig. 9 correspond to this magnetic-dipole transition.

The ionic energy levels can be split by the field of the surrounding lattice ions, i.e., by the crystal-field interaction. Since the 4*f* electrons are well screened from the environment, the crystal-field splitting for the 4*f* levels is much smaller. Now a level with J (I) = 0 is a single, non-degenerate state and cannot therefore be split. On the other hand, a level with $J = 1$ is triply degenerate and can be split. The manner of splitting depends on the symmetry of the crystal field.[26] A field possessing high symmetry does not cause splitting. Tetragonal or trigonal field causes splitting into two levels; crystal fields with lower symmetry as in SnO_2:Eu^{3+} (site symmetry = D_{2h}) cause splitting into three levels (Fig. 9).

In Fig. 9, the nearly structureless broad emission bands observed at ∼610 and ∼700 nm in β-Ga_2O_3 correspond to the $^5D_0 \rightarrow {}^7F_2$ and $^5D_0 \rightarrow {}^7F_4$ electric-dipole transitions, respectively. Note that the PL intensity ratio, ($^5D_0 \rightarrow {}^7F_2$) / ($^5D_0 \rightarrow {}^7F_1$), is an important factor indicating the concentration ratio of Eu^{3+} in the noncentrosymmetric to the centrosymmetric site. It has been shown from the large amount of tabulated data[27] that for totally symmetric sites its intensity ratio is lower than one, and increases to 10 for systems with very low symmetry sites. The β-Ga_2O_3:Eu^{3+} spectrum in Fig. 9 belongs to the latter case.

No clear $^5D_0 \rightarrow {}^7F_5$ structure, which should be expected to appear at ∼750 nm (Ref. 13), can be observed in any PL spectrum of Fig. 9. Under the assumption of negligible mixing by the even part of the crystal field, the theories of Judd and Ofelt (Refs. 28 and 29) show that the electronic dipole transitions from $J = 0$ to odd J levels are forbidden, and this is exemplified by the weakness of the transitions to $J = 3$ and 5 in Fig. 9 (see also Fig. 3). The transition to $J = 1$ is an exception because, as mentioned before, this line is magnetic dipole and obtains its intensity from the spin−orbit coupling of the ^5D and ^7F multiplets.

Effects of unintentionally doped Cr^{3+} ions.— It has been reported that an energy transfer from a lanthanide trivalent ion (Ce^{3+}, Eu^{3+}, Gd^{3+}, Tb^{3+}, Dy^{3+}, etc.) to the transition metal ion (Cr, Mn, Fe, Co, or Ni ion) in some phosphors, including Ga_2O_3, deteriorates the luminescence intensity of the lanthanide trivalent ion.[30–33] We can also expect from Fig. 3 that such deterioration effect of the trivalent ion luminescence occurs in our synthesized β-Ga_2O_3 phosphors. This is because of no strong emission intensity from the trivalent ions, especially from Tb^{3+} (Fig. 3b).

In Fig. 7, the Eu^{3+}-related $^5D_I \rightarrow {}^7F_J$ emission intensities tend to increase with increasing T for $T < 200$ K; conversely, the Cr^{3+}-originated R_1 intensity tends to decrease with increasing T for the same temperature range (i.e., $T < 200$ K). This fact suggests an evidence of energy transfer from Cr^{3+} to Eu^{3+} ($^7F_4$) at higher temperatures. In fact, the PLE spectra for the P_1 emission at $T = 300$ K (Fig. 6) showed a broad absorption band at ∼400 − 500 nm, which corresponds to the $^4A_2 \rightarrow {}^4T_1$ transitions in Cr^{3+}.

Van der Ziel and Van Uitert[17] reported an interesting coupled-ion process in the emission spectrum of Cr^{3+}-doped $Eu_3Ga_5O_{12}$. In addition to the well-known R lines in Cr^{3+} and the $^5D_0 \rightarrow {}^7F_J$ transition lines in Eu^{3+}, they observed lines which originate on the 2*E* level (Cr^{3+}), and terminate on the ^7F_J levels (Eu^{3+}). In our study, however, no such emission lines were identified. The reason for this may be (i) the Eu^{3+} ions in the present case are a dilute impurity in TGG, not those in the concentrated crystal (i.e., $Eu_3Ga_5O_{12}$) and (ii) the unintentionally doped Cr^{3+} concentration was too low to observe such unique Cr^{3+}−Eu^{3+} inter-ion coupling phenomena.

Finally, we can say that TGG is more efficient phosphor host for the lanthanide trivalent ion, Eu^{3+}, than β-Ga_2O_3. This is because even its smaller fractional composition efficient emission has been observed from the Ga_2O_3−TGG:Eu^{3+} mixture in Fig. 3d. Because the Cr^{3+}-originated R_1 and R_2 lines strongly interact with the Eu^{3+} states in the cubic TGG host, we can also say that the transition metal ion Cr^{3+} can also be preferentially doped into the cubic TGG host (Fig. 7). We note that the fractional TGG composition in the sample mostly used in this study ($M = 0.01$, $N = 0.0003$) was only $f_T \sim 0.06$ ($f_G \sim 0.94$; see Structural properties subsection in the Results section).

Conclusions

We synthesized Eu^{3+}-activated rare-earth gallium garnet phosphors (TGG:Eu^{3+}) by MOD and subsequent calcination treatment at $T_c = 1200°C$ for $t = 30$ min. The starting materials were a mixture of organic gallium solution and acetic acid dissolved with $TbCl_3$/Eu_2O_3. The XRD results revealed the synthesized phosphors to be a mixture of monoclinic Ga_2O_3 (β-Ga_2O_3) and cubic $Tb_3Ga_5O_{12}$ (TGG) crystallites. The effects of the $TbCl_3$/Eu_2O_3 addition on the structural and PL properties of the synthesized phosphors were investigated in detail. The effects of the Cr^{3+} ions, which were introduced as contaminants in the synthesized phosphors, on the PL properties were also studied by performing temperature-dependent PL measurements at $T = 20 - 380$ K and room-temperature PLE measurements. The MOD was shown to be the simplest technique to synthesize the high melting (∼1725°C) and high efficient rare-earth garnet (TGG) phosphor activated by the lanthanide trivalent ion (Eu^{3+}).

Acknowledgments

This work was supported by a Grant-in-Aid for Scientific Research (B) (26289085) and a Grant-in-Aid for Exploratory Research (25630120) from the Ministry of Education, Culture, Sports, Science

and Technology, Japan. The authors thank T. Miyazaki, T. Nakamura, and H. Oike for their experimental supports and useful discussion.

References

1. H. H. Tippins, *Phys. Rev.*, **140**, A316 (1965).
2. P. Wellenius, A. Suresh, and J. F. Muth, *Appl. Phys. Lett.*, **92**, 021111 (2008).
3. K. Sasaki, M. Higashiwaki, A. Kuramata, T. Masui, and S. Yamaskoshi, *IEEE Electron Device Lett.*, **34**, 493 (2013).
4. M. Higashiwaki, K. Sasaki, A. Kuramata, T. Masui, and S. Yamakoshi, *Appl. Phys. Lett.*, **100**, 013504 (2012).
5. C.-L. Hsu and Y.-C. Lu, *Nanoscale*, **4**, 5710 (2012).
6. H. Kim, C. Jin, S. An, and C. Lee, *Ceram. Int.*, **38**, 3563 (2012), and references therein.
7. K. Liu, M. Saurai, and M. Aono, *J. Mater. Chem.*, **22**, 12882 (2012).
8. W. Y. Weng, T. J. Hsueh, S.-J. Chang, G. J. Huang, and S. C. Huang, *IEEE Trans. Nanotechnol.*, **10**, 1047 (2011).
9. Z.-D. Huang, W.-Y. Weng, S.-J. Chang, Y.-F. Hua, C.-J. Chiu, T.-J. Hsueh, and S.-L. Wu, *IEEE Sens. J.*, **13**, 1187 (2013).
10. N. Ueda, H. Hosono, R. Waseda, and H. Kawazoe, *Appl. Phys. Lett.*, **70**, 3561 (1997).
11. Y. Hou, X. Wang, L. Wu, Z. Ding, and X. Fu, *Environ. Sci. Technol.*, **40**, 5799 (2006).
12. Y. Tokida and S. Adachi, *J. Appl. Phys.*, **112**, 063522 (2012).
13. Y. Tokida and S. Adachi, *Jpn. J. Appl. Phys.*, **52**, 101102 (2013).
14. Y. Tokida and S. Adachi, *ECS J. Solid State Sci. Technol.*, **3**, R100 (2014).
15. J. B. Gruber, D. K. Sardar, R. M. Yow, U. V. Valiev, A. K. Mukhammadiev, V. Y. Sokolov, I. Amin, K. Lengyel, I. S. Kachur, V. G. Piryatinskaya, and B. Zandi, *J. Appl. Phys.*, **101**, 023108 (2007), and references therein.
16. N. Zhuang, C. Song, L. Guo, R. Wang, X. Hu, B. Zhao, S. Lin, and J. Chen, *J. Cryst. Growth*, **381**, 27 (2013).
17. J. P. van der Ziel and L. G. Van Uitert, *Phys. Rev.*, **186**, 332 (1969).
18. S. Geller, *J. Chem. Phys.*, **33**, 676 (1960).
19. H. Sawada, *J. Solid State Chem.*, **132**, 300 (1997).
20. E. Nogales, B. Méndez, and J. Piqueras, *Appl. Phys. Lett.*, **86**, 113112 (2005).
21. E. Nogales, J. A. García, B. Méndez, and J. Piqueras, *J. Appl. Phys.*, **101**, 033517 (2007).
22. M. Toth and M. R. Phillips, *Appl. Phys. Lett.*, **75**, 3983 (1999).
23. S. Sugano and Y. Tanabe, *J. Phys. Soc. Jpn.*, **13**, 880 (1958).
24. T. Arai and S. Adachi, *J. Lumin.*, **153**, 46 (2014).
25. J. B. Gruber, U. V. Valiev, G. W. Burdick, S. A. Rakhimov, M. Pokhrel, and D. K. Sardar, *J. Lumin.*, **131**, 1945 (2011).
26. J. A. Koningstein, *Phys. Rev.*, **136**, A717 (1964).
27. R. Reisfeld, E. Zigansky, and M. Gaft, *Mol. Phys.*, **102**, 1319 (2004).
28. B. R. Judd, *Phys. Rev.*, **127**, 750 (1962).
29. G. S. Ofelt, *J. Chem. Phys.*, **37**, 511 (1962).
30. W. van Schaik, S. H. M. Poort, J. J. H. Schlotter, E. Dorrestijn, and G. Blasse, *J. Electrochem. Soc.*, **141**, 2201 (1994).
31. M. Yin, A. B. Yusov, A. M. Fedosseev, and J.-C. Krupa, *J. Phys.: Condens. Matter*, **14**, 8743 (2002).
32. G. Cabello, L. Lillo, Y. Huentupil, F. Cabrera, G. E. Buono-Core, and B. Chornick, *J. Phys. Chem. Solids*, **72**, 1170 (2011).
33. G. Cabello, L. Lillo, C. Caro, M. A. Soto-Arriaza, B. Chornik, and G. E. Buono-Core, *Ceram. Int.*, **39**, 2443 (2013).